

The effect of a Lorentz-force-driven rotating flow on the detachment of gas bubbles from the electrode surface

Weier, T.; Baczyzmalski, D.; Massing, J.; Landgraf, S.; Cierpka, C.;

Originally published:

August 2017

International Journal of Hydrogen Energy 42(2017)33, 20923-20933

DOI: <https://doi.org/10.1016/j.ijhydene.2017.07.034>

Perma-Link to Publication Repository of HZDR:

<https://www.hzdr.de/publications/Publ-25616>

Release of the secondary publication
on the basis of the German Copyright Law § 38 Section 4.

CC BY-NC-ND

The effect of a Lorentz-force-driven rotating flow on the detachment of gas bubbles from the electrode surface

Tom Weier^{a,*}, Dominik Baczyzmalski^{b,*}, Julian Massing^b, Steffen Landgraf^a,
Christian Cierpka^c

^a*Helmholtz-Zentrum Dresden - Rossendorf, Bautzner Landstraße 400, 01328 Dresden, Germany*

^b*Institut für Strömungsmechanik und Aerodynamik, Universität der Bundeswehr München, 85577 Neubiberg*

^c*Institut für Thermodynamik und Strömungsmechanik, Technische Universität Ilmenau, 98693 Ilmenau*

Abstract

Water electrolysis is a promising technique for energy conversion and is one of the key technologies to ensure an efficient and clean energy management in the future. However, the efficiency of this process is limited by overpotentials arising from - among other things - the high bubble coverage at the electrode surface. The influence of a magnetic field on the bubble behavior during electrolysis, in particular the bubble detachment from the electrodes, shows great potential for improving the efficiency of the process. In this study experiments and numerical simulations were carried out to investigate the effect of an electrode-normal magnetic field on the bubble detachment. Astigmatism Particle Tracking Velocimetry (APTV) was used to measure the magnetohydrodynamic (MHD) flow field around a magnetized sphere mimicking an electrolytic bubble. Complementary simulations gave further insight into the corresponding pressure field. The experimental and numerical results demonstrate that the pressure reduction formerly assumed to be responsible for the accelerated bubble detachment in the magnetic field is too weak to cause this effect. However, the flow over an arrangement of magnets was additionally measured by Particle Image Velocimetry (PIV), showing that the formation of bubble groups on the electrode surface gives rise to a stronger global flow which may have a substantial influence on the bubble behavior.

*Corresponding author. First and second author contributed equally to the paper.
Email addresses: t.weier@hzdr.de (Tom Weier),
dominik.baczyzmalski@unibw.de (Dominik Baczyzmalski)

1. Introduction

Currently, water electrolysis constitutes only 4% of the world hydrogen production, while the major part is generated from fossil fuels [1]. The generation of hydrogen from natural gas is with 1 Euro/kg much cheaper than its production by water electrolysis with approximately 6-10 Euro/kg. However, the possibility to power water electrolysis by renewable energy sources without producing greenhouse gases will eventually make this technique competitive in the future. Moreover, hydrogen is an excellent energy carrier with a high energy density and can be easily reconverted into electrical energy in a fuel cell. Thus, water electrolysis is considered as a key technology for an efficient energy management, which will be important in an energy economy that mainly depends on renewable sources. Among the different electrolyzer types that exist today, alkaline water electrolysis is the most mature and robust technology. It provides long lifetimes and does not rely on expensive cell materials or the need for high temperature handling, which makes this technique currently the most suitable option for the large-scale hydrogen production [2].

The minimum voltage to satisfy the energy demand required for the chemical reactions is referred to as the reversible cell voltage and amounts to $U_{\text{rev}} = 1.23$ V at standard conditions ($T = 298.15$ K, $p = 1$ bar). However, in reality additional losses arise due to reaction kinetics at the electrodes and ohmic losses. The cell voltage U_{cell} then calculates to

$$U_{\text{cell}} = U_{\text{rev}} + I \sum R + \Delta U_{\text{anode}} + \Delta U_{\text{cathode}}, \quad (1)$$

with $I \sum R$ accounting for the ohmic losses and ΔU_{anode} and $\Delta U_{\text{cathode}}$ denoting the anodic and cathodic overpotential, respectively [3]. Current alkaline water electrolyzers reach efficiencies up to 80-90% for high pressure (30 bar) and elevated temperatures (80 °C) [1]. However, for water electrolysis at atmospheric pressure and room temperature the efficiency reaches only 61-79%, depending on the effort taken for improving the performance. Particularly, at high current densities, i.e. high hydrogen production rates, the hydrogen and oxygen gas bubbles that are electrolytically generated at the respective electrodes significantly contribute to these losses, thus limiting the efficiency of the process and the operational current density [4]. As the void fraction in the cell becomes high with increasing current density, the effective conductivity of the bubble-filled electrolyte decreases and causes considerable ohmic losses [5, 6]. On the other hand, since large parts of the electrode

36 surface are covered by growing gas bubbles, the active electrode area is re-
 37 duced and the entire current has to pass through the remaining parts of
 38 the electrode, which leads to high reaction overpotentials [7, 8]. Therefore,
 39 reducing both the electrode bubble coverage and the void fraction is essen-
 40 tial to minimize the bubble-related losses and allow for higher efficiencies
 41 and hydrogen production rates. It has long been recognized that electrolyte
 42 motion can be useful to accelerate the transport of bubbles away from the
 43 interelectrode gap, thus decreasing the void fraction and the corresponding
 44 ohmic losses [5, 9, 10, 6]. In addition, it also helps to facilitate the bubble
 45 detachment and reduce the electrode bubble coverage [11, 12]. A simple and
 46 inexpensive method to generate electrolyte motion very close to the elec-
 47 trodes in order to enable an earlier bubble detachment is the application of
 48 magnetic fields. The superposition of a magnetic field on the inherent electric
 49 field produces Lorentz-forces $\mathbf{F} = \mathbf{j} \times \mathbf{B}$, where \mathbf{j} denotes the current den-
 50 sity and \mathbf{B} is the magnetic induction, respectively. These Lorentz-forces act
 51 directly as body forces in the fluid (electrolyte) and will generate electrolyte
 52 convection if they cannot be balanced by pressure.

53 The MHD flow generated by electrode-parallel magnetic fields was shown
 54 to effectively reduce the void fraction in the interelectrode gap and lower
 55 the bubble coverage on large electrodes with increasing magnitude of the
 56 magnetic field [13, 14, 15]. Moreover, a reduction of the ohmic losses and
 57 overpotentials as well as an improved process performance were reported
 58 in the magnetic field [16, 17, 18]. Koza et al. [19, 20, 15] investigated the
 59 effect of both an electrode-parallel and electrode-normal magnetic field at
 60 large planar electrodes and showed that both configurations were able to
 61 reduce the bubble detachment size and the fractional bubble coverage on the
 62 electrode. The earlier bubble detachment in an electrode-parallel magnetic
 63 field can be attributed to the strong shear flow generated by the Lorentz-
 64 forces [21, 22, 23, 24]. However, the underlying mechanisms occurring in an
 65 electrode-normal field are currently still under discussion [25, 26]. When an
 66 electrode-normal magnetic field is applied, the resulting Lorentz-force is zero
 67 in regions where the electric field and the magnetic field are parallel. Now,
 68 since a bubble acts as an electric insulator it causes a non-homogeneous
 69 current density distribution in its close proximity as schematically shown in
 70 Fig. 1 on the left side. This induces Lorentz-forces in azimuthal direction
 71 which drive a rotating flow around the bubble. Since the curvature of the
 72 electric field lines changes in sign in the lower part, the Lorentz-force will act
 73 in opposite direction above and below the bubble's equator. Moreover, the
 74 electrical field lines are stronger distorted on the upper part of the bubble,
 75 which leads to slightly stronger Lorentz-forces than close to the bottom.
 76 Thus, the Lorentz-force-driven rotating flow can be generally expected to be

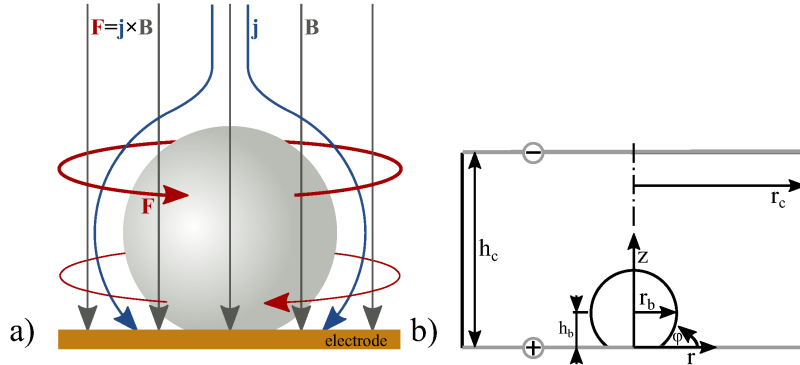


Figure 1: Sketch of the distribution of magnetic induction (\mathbf{B}), current density (\mathbf{j}), and Lorentz-force density (\mathbf{F}) in the vicinity of an electrolytic bubble in an electrode parallel magnetic field (left). Coordinate system and designations of the problem (right).

77 faster above the bubble equator than below. To explain the faster detachment
 78 of the bubbles in such a configuration, it was suggested that the resulting
 79 flow forms a region of lower pressure above the bubble. This imposes a force
 80 acting in favor of the bubble detachment and thus could explain the reduced
 81 detachment size observed in the electrode-normal magnetic field [15].

82 To pursue this assumption and gain further insight on how to optimize the
 83 magnetic field arrangements, a better understanding of the complex three-
 84 dimensional flow around the evolving bubbles is necessary. However, it is
 85 almost impossible to experimentally investigate the flow around real individ-
 86 ual bubbles growing on large electrode since many bubbles may form simul-
 87 taneously at random places all over the electrode. An alternative approach
 88 chosen by many researches is to use nano- [27] or microelectrodes (diameter
 89 $\sim O(100 \mu\text{m})$) in order to pin the bubbles at a certain position which can be
 90 investigated by optical means [26, 28, 29, 30, 31]. In contrast to the obser-
 91 vations at large electrodes, the experimental and numerical results reported
 92 in these studies point to a stabilizing effect of the electrode-normal magnetic
 93 field, i.e. an increase of the detachment size. The opposite behavior can be
 94 attributed to the strong difference of the Lorentz-force distribution. Since
 95 the entire current has to pass through the much smaller microelectrode, the
 96 current density and the Lorentz-forces are much stronger at the bottom than
 97 at the top of the bubble. This gives rise to a lower pressure in the lower part
 98 of the bubble as opposed to the case at large electrodes and may explain
 99 the stabilizing effect [26, 25]. Nonetheless, the reported gas bubble behavior
 100 on microelectrodes cannot be directly transferred to the realistic case of gas
 101 bubbles on macroelectrodes as the Lorentz-force distributions in both cases

102 are by no means comparable.

103 The aim of the current study is to provide further insight into the complex
104 MHD flow generated by an electrode-normal magnetic field and clarify the ef-
105 fect of the hydrodynamic force on the bubble detachment at large electrodes.
106 Since the bubbles form at random places it is not possible to conduct detailed
107 flow measurements around a single bubble at a large electrode, therefore a
108 magnetized sphere is used here instead. This setup enables to mimic a single
109 stationary electrolytic gas bubble on a macroelectrode with an equivalent
110 Lorentz-force distribution. The three-dimensional electrolyte flow around
111 the magnetic sphere was experimentally resolved using Astigmatism Particle
112 Tracking Velocimetry for the first time. These measurements are supported
113 by additional numerical simulations, which allowed for the calculation of the
114 hydrodynamic forces that are imposed on the sphere or bubble by the MHD
115 flow. In addition, Particle Image Velocimetry (PIV) measurements were con-
116 ducted in a second setup employing an arrangement of multiple magnets in
117 order to study the global MHD flow that is formed in the case of bubble
118 groups as opposed to single bubbles.

119 2. Experimental setup

120 Given the rotational symmetry of the MHD flow around a single sphere in
121 an electrode-normal magnetic field (see Fig. 1 right), a cylindrical electrolysis
122 cell with an inner diameter of 35.6 mm was used for the measurements as
123 shown in Fig. 2. The cell was made from Plexiglass to allow for optical
124 access from the side walls. The working electrode consists of pure copper
125 and formed the bottom of the cell, whereas a Cu ring electrode placed on the
126 top of the cell served as counter electrode. This allowed for an undisturbed
127 observation of the measurement volume from the top. At the bottom of the
128 cell an axially magnetized NdFeB sphere with a diameter of 10 mm was placed
129 onto a plastic pillar with a height of 8 mm. Using this magnetized sphere
130 the same Lorentz-force distribution as in the case of a stationary spherical
131 gas bubble at a large electrode in an electrode-normal magnetic field can be
132 generated as will be explained in the following. The magnetic field in an
133 infinite domain outside ($r > r_b$) of a spherical magnet with magnetization
134 M_0 is given by [32]

$$\begin{aligned} B_r &= \frac{2}{3} M_0 \frac{r_b^3}{r^3} \cos \theta \\ B_\theta &= \frac{1}{3} M_0 \frac{r_b^3}{r^3} \sin \theta \end{aligned} \quad (2)$$

135 Here, r , θ , φ are spherical coordinates originating at the center of the sphere
136 and r_b is the radius of the sphere. Similarly, the electric field around a

137 spherical insulator in an infinitely extended space can be written as [33]

$$\begin{aligned}
 E_r &= E_0 \left(1 - \frac{r_b^3}{r^3} \right) \cos \theta \\
 E_\theta &= -E_0 \left(1 + \frac{r_b^3}{2r^3} \right) \sin \theta
 \end{aligned}
 \tag{3}$$

138 From Eq. (2) and Eq. (3) the Lorentz-force distribution around an electrically
 139 insulating spherical magnet results as

$$f_{L,M} = \sigma_e \mathbf{E} \times \mathbf{B} = \sigma_e E_0 M_0 \frac{r_b^3}{r^3} \sin \theta \cos \theta \mathbf{e}_\varphi
 \tag{4}$$

140 On the other hand, the Lorentz-force distribution around an insulating (and
 141 non-magnetic) sphere in a uniform vertical magnetic field B_z follows as

$$f_{L,B} = -\frac{3}{2} \sigma_e E_0 B_z \frac{r_b^3}{r^3} \sin \theta \cos \theta \mathbf{e}_\varphi.
 \tag{5}$$

142 Note that the Lorentz-force distributions solely possess an azimuthal (φ)
 143 component and for both cases differ only by a constant factor. Identical
 144 Lorentz-force distributions for $f_{L,M}$ and $f_{L,B}$ result if

$$B_z = -\frac{2}{3} M_0
 \tag{6}$$

145 However, to ensure the same Lorentz-force distribution as for the case of
 146 an insulating sphere the magnetic sphere could not be placed directly on the
 147 electrode but had to be lifted from the ground. The Lorentz-force distribution
 148 is generally confined to the vicinity of the sphere, although the ring electrode
 149 also creates strong distortions of the current field in the upper part of the cell.
 150 The magnetic field is already very weak in this region and thus the generated
 151 Lorentz-forces can be neglected. Since the elevated magnetic sphere cannot
 152 account for the effect of the bottom wall, the case of an insulating sphere
 153 directly attached to the electrode will be additionally considered in a second
 154 set of numerical simulations (see Sec. 3).

155 The cell was filled with a 1 M Cu_2SO_4 solution as an electrolyte, which
 156 ensured in conjunction with the pure copper electrodes that a current field
 157 is established even below the decomposition voltage of water. It should be
 158 mentioned that local density gradients will be created in the electrolyte with
 159 time due to the dissolution and deposition of copper. However, since the
 160 bottom electrode was used as the anode, copper was only dissolved at the
 161 bottom of the cell, which leads to a stable stratification. The experiments

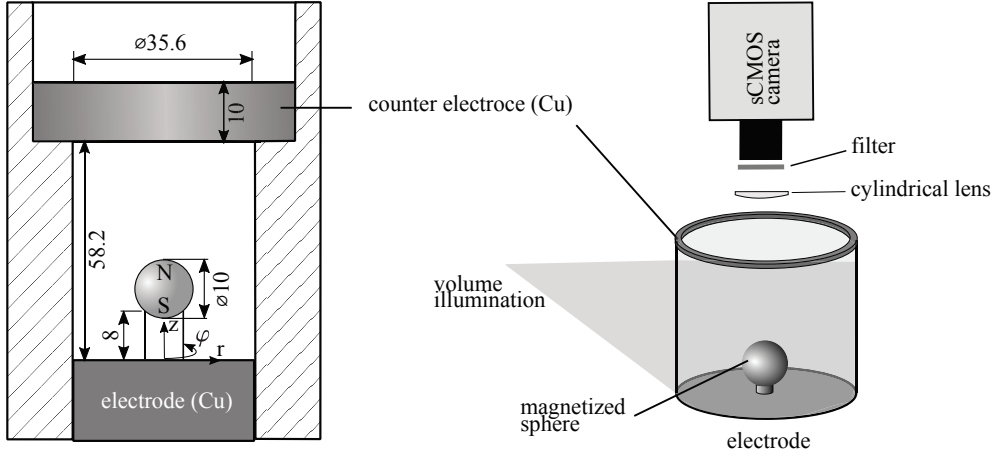


Figure 2: Sketch of the electrochemical cell employing a magnetized sphere (left) and the corresponding APTV measurement setup (right).

162 were carried out under galvanostatic conditions, i.e. using a constant current
 163 supply. Different values of the electric current were applied in successive
 164 experiments in order to vary the magnitude of the Lorentz-force ($f_L \sim jB$).
 165 Here, a current of $I = 30, 60, 90, 120$ and 150 mA was used, which yields a
 166 current density at the surface of the working electrode of about $j = 30, 60,$
 167 $90, 120$ and 150 Am^{-2} . The magnetization of the sphere amounts to 1 T, thus
 168 generating a Lorentz-force distribution that is equivalent to that induced
 169 by an uniform electrode-normal magnetic field of $B_z = 0.66$ T according to
 170 Eq. (6). Altogether, the magnitude of the resulting Lorentz-forces is in good
 171 agreement with the experiments by Koza et al. [15].

172 A sketch of the experimental setup is shown on the right side of Fig. 2.
 173 All three components of the three-dimensional velocity field (3D3C) around
 174 the elevated magnetized sphere were measured by means of Astigmatism
 175 Particle Tracking Velocimetry [APTV, see 34]. This is a special single-camera
 176 particle tracking technique in which a cylindrical lens is placed in front of
 177 the camera to disturb the axis-symmetry of the optical system and causes
 178 astigmatic aberrations. The particle images will appear elliptical, where
 179 the size of the major and minor axes unambiguously depend on the actual
 180 depth position in the measurement volume. By a proper image processing
 181 and calibration this can be correlated with the actual depth position of the
 182 particle [35]. Fluorescent polystyrene particles (FluoRed by Microparticles
 183 GmbH) with a diameter of $50 \mu\text{m}$ served as flow tracers. Even though these
 184 particles are relatively large, they do not suffer from fast sedimentation, since
 185 their density is very close to that of the electrolyte ($\rho_{\text{Cu}_2\text{SO}_4} \approx 1.05 \text{ gcm}^{-3}$,
 186 $\rho_{\text{particle}} \approx 1.06 \text{ gcm}^{-3}$). A pulsed Nd:Yag laser with a wave length of 532 nm

187 and a pulse energy of 15 mJ was used as a light source. The laser beam was
 188 passed through a beam expander via an optical fiber and illuminated the
 189 entire cell. The images were captured from the top at a frame rate of 15 Hz by
 190 a sCMOS camera (Imager sCMOS, LaVision GmbH) and a Zeiss $f = 50$ mm
 191 macro-planar objective. Two laser pulses without time delay were shot in
 192 each frame, to increase the illumination intensity. A 532 nm notch filter was
 193 mounted on the objective to only transmit the fluorescent light emitted by
 194 the tracer particles and avoid the strong laser reflections from the copper
 195 surface. Moreover, a cylindrical lens with a focal length of $f = 300$ mm was
 196 placed in front of the camera to create astigmatic distortions of the particle
 197 images. The resulting measurement volume extended over the entire inner
 198 diameter of the electrolysis cell, from the bottom of the cell ($z = 0$ mm)
 199 to a height of $z \approx 40$ mm. The velocity was reconstructed from the three-
 200 dimensional particle positions by determining the particle trajectories with
 201 a time-resolved tracking algorithm. Moreover, the trajectories were locally
 202 fitted by a second order polynomial fit for a higher accuracy [36]. Since
 203 the MHD flow is steady and rotationally symmetric, the velocity data was
 204 averaged over the whole circumference into one meridional (rz) plane. The
 205 corresponding bin size was 0.5×0.5 mm².

206 3. Numerical Simulations

207 The finite volume library OpenFOAM licensed under the GNU General
 208 Public Licence [37] was used to perform the computations. To incorporate
 209 the electromagnetic body force, the solver simpleFoam of OpenFOAM version
 210 1.7.x was extended by a Lorentz-force term. Under the conditions considered
 211 here, this term can be pre-computed and does neither depend on time nor on
 212 the flow. This is not immediately clear from Ohm's law for moving conductors

$$\mathbf{j} = \sigma(\mathbf{E} + \mathbf{v} \times \mathbf{B}) \quad (7)$$

213 that - besides the conventional proportionality to the electric field \mathbf{E} - relates
 214 the current density to an induction term $\mathbf{v} \times \mathbf{B}$ depending on velocity \mathbf{v} and
 215 magnetic field \mathbf{B} . However, the electrolyte's electrical conductivity σ is quite
 216 small and velocities as well as magnetic field magnitudes are moderate. For
 217 this reason, the electric currents induced by the electrolyte motion and even
 218 more so the magnetic fields of the induced currents can safely be neglected
 219 compared to the applied electric and magnetic fields. Therefore, the calcu-
 220 lation of the Lorentz-forces can be decoupled from solving the Navier-Stokes
 221 equations.

222 Current distributions were always determined numerically in order to ac-
 223 count for additional insulating parts such as the pillar tethering the sphere,

224 even if the analytical expression was used for the magnetic field of the magne-
 225 tized sphere. The electric field \mathbf{E} was computed by solving a Laplace equation
 226 for the electric potential using the OpenFOAM solver `laplacianFoam`. Fixed
 227 potentials were set at the top and the bottom of the cell such as to match the
 228 desired cell current. The vertical boundaries as well as the bubbles surface
 229 were treated as insulating, i.e., no normal currents were allowed there. The
 230 current density distribution then results simply from the gradients of the
 231 electric potential times conductivity.

232 Two slightly different setups were used for the comparison with the exper-
 233 iment (Figs. 4, 5) on the one hand and to determine the scaling of the forces
 234 (Fig. 6) on the other hand. That means, the first configuration is based on
 235 the experiment using the tethered magnetized sphere as discussed in the pre-
 236 vious section. Validated by the experimental data, these simulations formed
 237 the groundwork for the computation of the more bubble-growth-like case of
 238 an insulating sphere that is directly attached to the electrode. This way, the
 239 effect of the electrode on the current distribution and the influence of the
 240 solid wall on the flow can also be accounted for. For the latter case, a homo-
 241 geneous magnetic field in vertical direction was combined with the electric
 242 field obtained from the Laplace equation.

243 In both cases, the two-dimensional Navier-Stokes equations with body
 244 force term were solved on an axis-symmetric structured grid. A mesh with
 245 approximately 2.5×10^5 hexahedral cells and highest resolution in the vicinity
 246 of the sphere was used for the tethered sphere geometry of Fig. 2. The
 247 parameter studies depicted in the right diagram of Fig. 6 were conducted
 248 under the assumption of a constant aspect ratio between cell and bubble,
 249 while the cell radius amounted to four times the bubble radius and the cell
 250 height was twelve times the radius of the bubble.

251 4. Results and discussion

252 4.1. Forces

253 The detachment of the bubble from the electrode surface depends on the
 254 forces that are acting on it. The prevailing forces that are usually considered
 255 in this context are the buoyancy F_B , the surface tension force F_γ and the
 256 hydrodynamic forces, here referred to as $F_{\Delta p}$ (see Fig. 3). The buoyancy force
 257 acts in favor of the the bubble detachment and increases with the bubble size
 258 according to

$$F_{Bz} = (\rho_l - \rho_g) V g = (\rho_l - \rho_g) \frac{\pi}{6} d^3 g, \quad (8)$$

259 where ρ_g and ρ_l , are the density of the gaseous phase (bubble) and the liquid
 260 phase (electrolyte), respectively, V denotes the bubble volume, d is the bubble

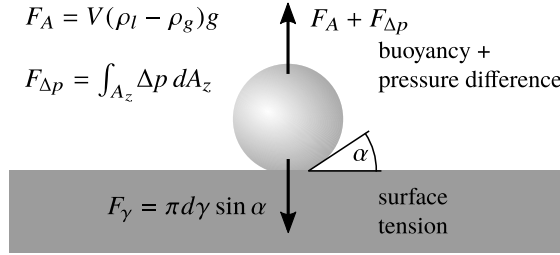


Figure 3: Sketch of the forces acting on a bubble at a horizontal electrode.

261 diameter and g the gravitational acceleration. The surface tension force F_γ ,
 262 on the other hand, is responsible for keeping the bubble attached to the
 263 surface. For the simple case of a bubble adhering to a horizontal surface in
 264 a rotationally symmetric flow, the resulting force can be written as

$$F_{\gamma z} = -\pi d_c \gamma \sin \alpha, \quad (9)$$

265 where α denotes the contact angle, γ is the gas-liquid surface tension and d_c
 266 is the contact diameter of the bubble with the wall,

267 Since a stationary sphere is considered here, no hydrodynamic drag is
 268 imposed. The only relevant hydrodynamic force that needs to be considered
 269 in the present case is related to the MHD-induced relative pressure change
 270 along the surface of the sphere, which yields for the z -direction

$$\mathbf{F}_{\Delta p} = - \int_{A_z} (p_l - p_c) dA_z, \quad (10)$$

271 where $\Delta p = p_l - p_c$ is the hydrodynamic pressure of the liquid relative to the
 272 reference pressure at the contact line and A_z is the bubble surface projected
 273 in z -direction. In a stagnant liquid the bubble will generally stay attached to
 274 the surface until the bubble size and thus its buoyancy becomes sufficiently
 275 large to overcome the surface tension force. In the presence of an electrode-
 276 normal magnetic field, the MHD-induced pressure force $F_{\Delta p}$ might facilitate
 277 its detachment. Based on the numerical results $F_{\Delta p}$ will be compared to the
 278 buoyancy force F_B in order to assess the effect of the MHD-induced pressure
 279 change on the bubble detachment.

280 4.2. Flow fields

281 The flow fields are qualitatively very similar for the different investigated
 282 currents. Therefore, only the flow field at $I = 60$ mA is considered here for a
 283 detailed discussion. Fig. 4 shows all three mean velocity components in the

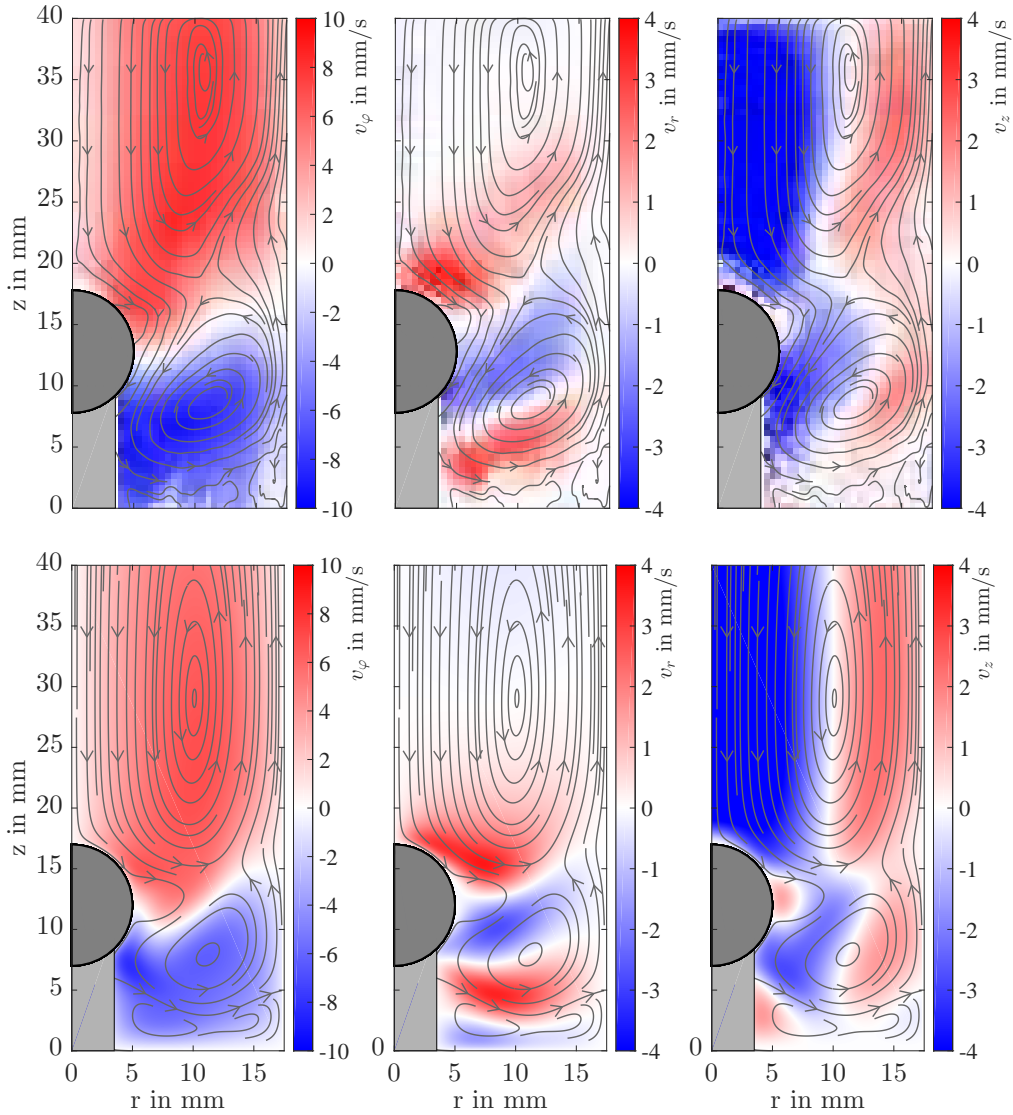


Figure 4: Experimentally (top) end numerically (bottom) obtained velocity field around the magnetized sphere in the rz -plane. The grid size for representation of the data is 0.5 mm and 0.25 mm in each direction for the experimental and numerical data, respectively. Circumferential velocity (left), radial velocity (middle) and axial velocity (right). The streamlines (grey) were added to better visualize the in-plane velocity field in the meridional (rz) plane.

284 meridional rz -plane together with stream lines of the secondary (in-plane)
 285 flow for the experiment (top) and the simulation (bottom). The azimuthal
 286 velocity v_φ is shown on the left, the radial velocity v_r in the middle and the
 287 axial/vertical velocity v_z on the right. As can be seen from the azimuthal
 288 velocity distribution (left side of Fig. 4), the experimental and numerical

289 data is in very good agreement. As expected, the Lorentz-forces give rise
 290 to a rotating flow with different sign on the upper and lower side of the
 291 sphere. This is different to the case of a microelectrode, where the Lorentz
 292 forces are dominant on the lower side of the bubble due to the high current
 293 density and no counter-rotating flow could be observed on the upper side [26].
 294 Since the magnetized sphere is elevated, the bending of the electric field lines
 295 is in the same order of magnitude on both sides of the sphere and thus
 296 the Lorentz forces are also relatively similar in this case. In the region of
 297 the sphere ($8.5 \text{ mm} \leq z \leq 18.5 \text{ mm}$), the magnitude of the azimuthal flow
 298 above the sphere is indeed slightly larger ($\sim 10\%$) than in the lower part
 299 of the sphere as expected from the theoretical field distribution (Fig. 1).
 300 Furthermore, the average position of the shear layer between the counter-
 301 rotating flow regions is not horizontally aligned, but follows a curved path
 302 which is inclined upwards in radial direction and shows a minimum at $r =$
 303 7 mm and $z = 10 \text{ mm}$. It can be also seen that the Lorentz-force-induced
 304 flow is not limited to the vicinity of the sphere but the fluid rotates in the
 305 entire cell due to viscous effects. Moreover, the azimuthal velocities increase
 306 with the applied current density as is shown on the right side of Fig. 5 for the
 307 maximum measured velocity in the cell. It can be seen that the maximum
 308 velocity increases approximately with the square root of the current density,
 309 $v_\varphi \sim \sqrt{j}$, which can be attributed to the fact that the dynamic pressure
 310 is directly related to the imposed Lorentz forces, i.e. $\frac{\rho}{2}v_\varphi^2 \sim jBd$ (d is the
 311 diameter of the sphere representing a characteristic length scale).

312 The azimuthal fluid motion will obviously give rise to centrifugal forces,
 313 which in turn will cause the pressure to increase toward the outer wall.
 314 Since the azimuthal velocity is the predominant flow component, the pressure
 315 change can be estimated by

$$\frac{\partial p}{\partial r} = \rho \frac{v_\varphi^2}{r}. \quad (11)$$

316 This is exemplified on the left side of Fig. 5, where the radial distribution
 317 of the azimuthal velocity and the corresponding relative pressure change are
 318 illustrated in a horizontal plane slightly above the sphere (numerical results).
 319 The relative pressure distribution obtained by integrating the velocity profile
 320 according to Eq. (11) is generally in good agreement with the distribution
 321 directly obtained from the numerical simulation. Differences occur within
 322 the inner region for $r < 5 \text{ mm}$) directly above the sphere due to the action
 323 of the secondary flow as discussed below.

324 In the middle and right column of Fig. 4 the secondary flow in the merid-
 325 ional plane is shown and additionally highlighted by the streamlines. Due to
 326 the centrifugal force caused by the azimuthal motion above and below the
 327 sphere, the fluid is forced to move toward the outer part of the cell as indi-

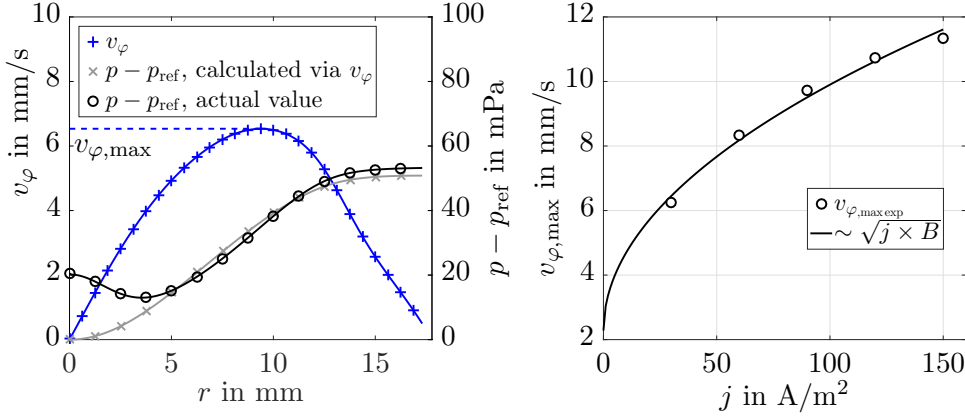


Figure 5: Radial distribution of v_ϕ and the relative pressure $p - p_{\text{ref}}$ in a horizontal plane located 1 mm above the sphere obtained from the simulations at $j = 60 \text{ A/m}^2$ (left). Maximum measured azimuthal velocity v_ϕ in the cell vs. the applied current density j (right).

328 cated by the red color in the representation of v_r . In the shear layer, where
 329 the azimuthal velocity and the centrifugal forces are rather small, the fluid
 330 flows back from the outer parts due to continuity. The numerical data shows
 331 that such inward directed flow is also evident close to the bottom of the cell.
 332 This can similarly be attributed to the low centrifugal momentum in the wall
 333 boundary layer which cannot withstand the elevated pressure in the outer
 334 cell region [see 38]. Since measurements close to the wall are subjected to a
 335 higher noise level, this effect cannot be seen in the experimental data.

336 The distribution of the axial velocity v_z is again in very good agreement
 337 between the experimental and numerical results. Above the sphere a large
 338 flow region is directed toward the sphere (indicated by the blue color, $v_z \approx$
 339 -5 mms^{-1}). This is a consequence of the lower pressure in the center of the
 340 cell caused by the rotating motion. Due to the impingement of this flow on
 341 the upper part of the sphere the pressure reduction in this region is weaker
 342 compared to the case where only the action of azimuthal flow is considered
 343 as previously shown on the left side of Fig 5. After approaching the sphere
 344 the fluid is accelerated outwards due to the centrifugal forces as explained
 345 before. Finally, the fluid has to flow upwards at the outer part of the cell
 346 due to continuity. Since the available area becomes larger with increasing
 347 radius, the absolute velocity of the upward flow in the outer part is smaller
 348 ($v_z \approx 2 \text{ mms}^{-1}$) compared to the downward flow in the inner part. It is
 349 also interesting to note that the portion of fluid moving downward along the
 350 sphere detaches from the sphere close to the equator at $r \approx 5 \text{ mm}$ and z
 351 $\approx 12 \text{ mm}$, as indicated by the small region of upward moving motion. The

352 resolution of the experimental data is high enough to show the same feature,
 353 although to a smaller extent.

354 4.3. The hydrodynamic lift force

355 As suggested by Koza et al. [15] the higher azimuthal flow velocities on
 356 the upper side of the sphere will lead to a lower pressure in comparison to
 357 the lower side of the bubble. The result of such a pressure distribution is a
 358 hydrodynamic lift force that may facilitate the bubble detachment. However,
 359 as was shown before in Fig. 5 the pressure change induced by the azimuthal
 360 fluid motion is relatively small (< 50 mPa). By comparison, the hydrostatic
 361 pressure change around the sphere is $\Delta p = \rho g d \approx 100$ Pa. Thus, irrespective
 362 of the additional action of the secondary flow, the Lorentz-force-induced lift
 363 force can be expected to be several orders of magnitude lower than the buoy-
 364 ancy force. However, since the size of electrolytically generated hydrogen or
 365 oxygen gas bubbles is much smaller than that of the investigated sphere, it
 366 is important to understand how the respective forces scale with the diameter
 367 of the bubble. According to Eq. (11) the MHD-induced pressure change can
 368 be written as $\Delta p \sim \rho v_\varphi^2$. Moreover, the velocity scales approximately with
 369 $v_\varphi \sim \sqrt{j B d}$ as discussed before (see also Fig. 5, right). The MHD-induced
 370 pressure change can be therefore related to the Lorentz forces by

$$\Delta p \sim \rho v_\varphi^2 \sim j B d. \quad (12)$$

371 The resulting pressure-induced lift force can be then estimated according to

$$F_{\Delta p} \sim \Delta p \frac{\pi}{4} d^2 \sim j B d^3. \quad (13)$$

372 Thus, the generated lift force scales with d^3 . Now, since the buoyancy of a
 373 gas bubble ($F_{Bz} \sim (\rho_l - \rho_g) g d^3$) also scales with d^3 , the ratio between the
 374 lift force and the buoyancy force can be expected to be independent of the
 375 bubble size in a first approximation.

376 To support these findings, the imposed lift force can be directly calcu-
 377 lated from the numerical simulations. To include the effect of the electrode
 378 on the Lorentz force distribution and the MHD flow, which was not cor-
 379 rectly reproduced by the elevated magnetized sphere, the more realistic case
 380 of an insulating sphere directly attached to the electrode will be considered
 381 here. Fig. 6 shows the corresponding flow field, visualized by the three-
 382 dimensional streamlines colored by their velocity magnitude. In addition,
 383 pressure contours are shown in the meridional plane (rz -plane). The lift
 384 force $F_{\Delta p}$ calculated from this pressure distribution at different values of the
 385 sphere's diameter is shown on the right side of Fig. 6 together with the cor-
 386 responding buoyancy force and the Reynolds number. The magnitude of the

387 simulated Lorentz forces was relatively small ($f_L \sim jB = 3.33 \text{ Nm}^{-3}$), but
 388 still exceeds that used in the parallel fields experiment of Koza et al. [15] by
 389 about an order of magnitude. As can be seen, the hydrodynamic lift force $F_{\Delta p}$
 390 is in the order of 10^{-7} N for a diameter of 10 mm and is approximately four
 391 orders of magnitude lower than the buoyancy force. As expected from the
 392 theoretical discussion, the $F_{\Delta p} \sim d^3$ dependency is generally evident. How-
 393 ever, as the diameter is reduced the reduction of the lift force becomes even
 394 stronger due to viscous effect which become more relevant at low Reynolds
 395 numbers. Consequently, the MHD-induced lift force is unlikely to be the rea-
 396 son for the reduction of the bubble detachment diameter observed by Koza
 397 et al. [19, 20, 15] in an electrode-normal magnetic field.

398 On the other hand, for much higher current densities in the order of
 399 10 kAm^{-2} and magnetic fields of $B \approx 1 \text{ T}$ ($jB = 10 \text{ kNm}^{-3}$), which are re-
 400 alistic conditions for practical applications, the lift force may have a more
 401 significant contribution. However, at high current densities the bubble cov-
 402 erage on the electrode surface and the void fraction becomes very high, so
 403 that the interaction between the bubbles would also have to be taken into
 404 account. In fact, even at low current densities and electrode bubble coverage
 405 the interaction between the MHD flow around the individual bubbles could
 406 lead to relevant flow effects as discussed in the next section.

407 4.4. Multiple magnets

408 In contrast to the MHD flow around single bubbles, the resulting MHD
 409 flow around a group of bubbles might give an alternative explanation of
 410 the earlier bubble release under magnetic field influence observed by Koza et
 411 al. [15]. Fig. 7 shows two different arrangements of nine cylindrical permanent
 412 magnets made of NdFeB (Fig. 7a, Fig. 7d) fixated below a 0.5 mm thick
 413 Pt foil used as cathode. A single magnet had a diameter and height both
 414 of $H = 3 \text{ mm}$. The cell's diameter and height were 40 mm and 50 mm,
 415 respectively. The cell was filled with an aqueous solution of 0.9 M CuSO_4
 416 and 1.5 M H_2SO_4 . Current flows from a 10 mm high Cu anode mounted
 417 to the inner rim on top of the cell towards the cathodic Pt plate on the
 418 bottom of the cell. The arrangement is quite similar to the setup shown in
 419 Fig. 2. Since the magnetic fields of the upper poles of the permanent magnets
 420 penetrate the Pt foil circumferential Lorentz-forces are generated atop of each
 421 single magnet as sketched between Fig. 7b and Fig. 7c. Depending on the
 422 magnetization direction, the Lorentz-force is directed either clockwise (north
 423 pole on top) or counter-clockwise (south pole on top).

424 For the following discussion, a coordinate system originating at the cells
 425 center at the upper surface of the Pt foil will be used. z is the vertical co-
 426 ordinate. The flow was measured with conventional PIV in horizontal slices

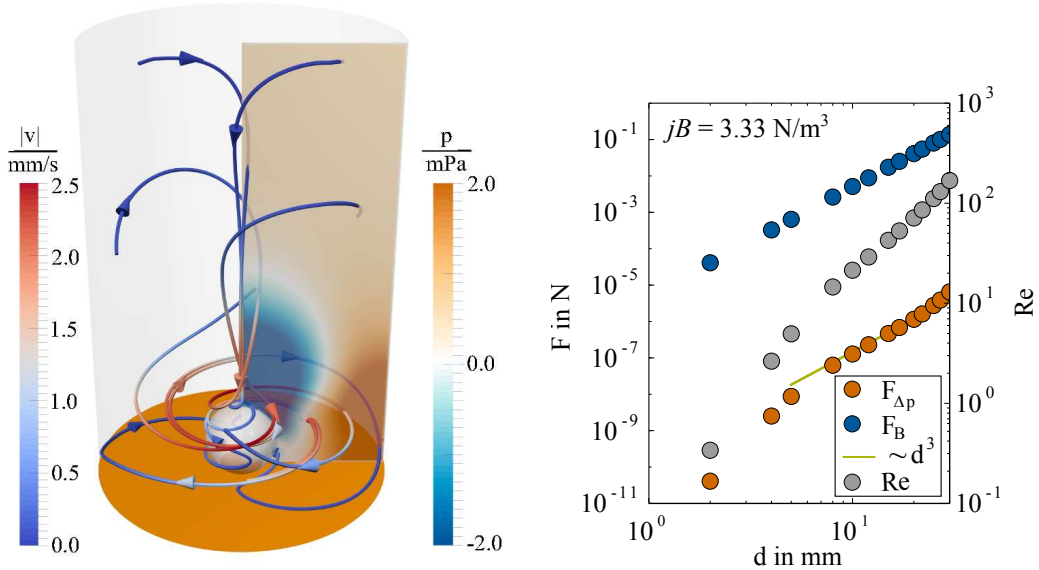


Figure 6: Rotating MHD flow around an insulating sphere obtained from numerical simulation with streamlines colored by the velocity magnitude and the pressure contour illustrated in the meridional plane (left). Hydrodynamic lift force, buoyancy and Reynolds number calculated for different diameters (right).

427 of constant z . Therefore, the velocity magnitude ($|v|$) contains only veloc-
 428 ity components in the horizontal plane. In the checkerboard arrangement
 429 (Fig. 7a, b, e, f) the forces generated by the single magnets add up in the
 430 inter-magnet spaces. Accordingly, a relatively regular flow develops directly
 431 above the magnet array at $z = 1$ mm (Fig. 7e) closely tracing the magnet
 432 contours. Slightly farther away from the cathode only a weak and barely de-
 433 tectable motion remains ($z = 5$ mm, Fig. 7f). Essentially, the checkerboard
 434 arrangement of the permanent magnets leads to a locally intense flow limited
 435 to the direct vicinity of the cathode. Further away some weak motions are
 436 still detectable, but no large scale flow is driven.

437 In contrast, an array of magnets with parallel magnetization directions
 438 (Fig. 7d) generates unidirectional rotation around the poles. In this case
 439 forces originating from the single magnets are opposing in the inter-magnetic
 440 spaces and partially cancel each other out (Fig. 7c). However, along the
 441 outer rim of the magnet array the Lorentz-forces from single magnets have
 442 the same (in the current case counter-clockwise) direction and add up. This
 443 situation is comparable to the summation of the magnetization currents in
 444 a volume, where only the surface magnetization currents contribute to the
 445 macroscopic field (c.f., e.g., [39]). The force configuration in Fig. 7d re-

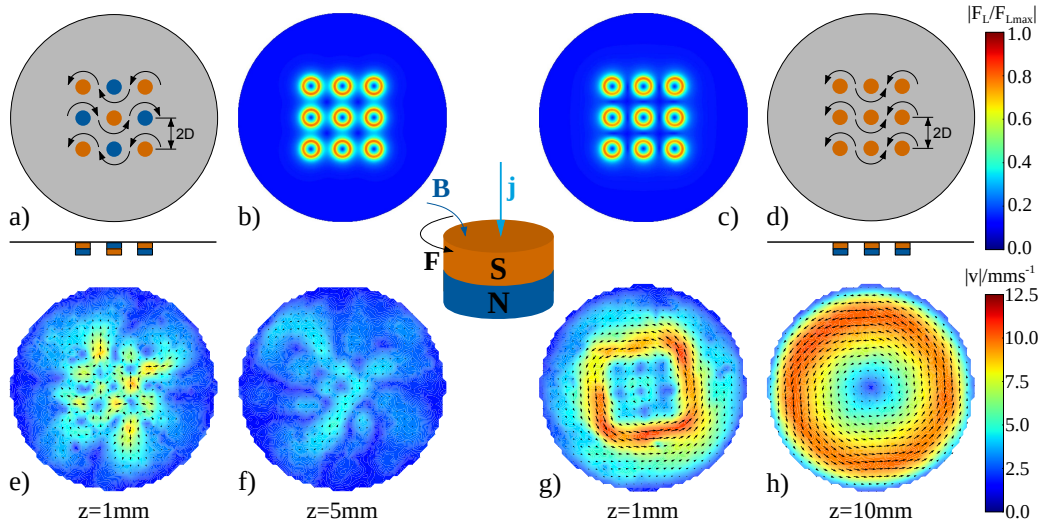


Figure 7: Lorentz-force distribution and flow generated by multiple magnets with magnetization directions all parallel (rightmost two columns) or in a checkerboard arrangement (leftmost two columns). A single magnet has a diameter $D = 3$ mm and a height $H = 3$ mm, the cell diameter and height are 40 mm and 50 mm, respectively. Current densities of 380 Am^{-2} and 360 Am^{-2} were applied to the checkerboard (e, f) and the parallel (g, h) arrangement, respectively.

446 sembles that originating from a group of bubbles on a larger electrode. The
 447 direction of the azimuthal force around single bubbles is the same, so Lorentz-
 448 forces are weakened in the inter-bubble spaces but sum up around the bubble
 449 collective. Returning to the magnets, at $z = 1$ mm (Fig. 7g) the electrolyte
 450 flows around the array following roughly the counter-clockwise Lorentz-forces
 451 along the eight outer magnets. The rectangular shape of the maximum ve-
 452 locity contour is tilted somewhat in flow direction with respect to the magnet
 453 array. Inside the array, velocities are much lower compared to those observed
 454 for the checkerboard pattern (c.f., Fig. 7e). In stark contrast to the checker-
 455 board arrangement, the counter-clockwise Lorentz forces along the magnet
 456 array lead to an intense global flow spanning a large volume as can be seen
 457 from the horizontal cut at $z = 10$ mm in Fig. 7h. Applied to multiple bubbles
 458 on an electrode this would mean that such a strong flow exerts drag forces on
 459 the bubbles acting mainly in electrode parallel direction. These drag forces
 460 could set the bubbles in sliding motion along the surface and support their
 461 earlier detachment.

462 5. Summary and conclusions

463 The aim of the current study was to investigate if the pressure change
464 induced by the MHD flow in an electrode-normal magnetic field can signifi-
465 cantly alter the detachment process of the bubble as hypothesized by Koza et
466 al. [19, 20, 15]. Therefore, the complex three-dimensional flow around a mag-
467 netized sphere ($d = 10$ mm), mimicking an electrolytic gas bubble produced
468 at a planar electrode was measured by astigmatism particle tracking. In or-
469 der to gather the pressure information both the case of a magnetized sphere
470 and an insulated sphere under the influence of a homogeneous magnetic field
471 were investigated numerically.

472 The comparison between the numerical simulation and the experiment
473 shows a very good agreement. Based on the numerical simulations, it could
474 be shown that the MHD-induced lift force is too small to explain the accel-
475 erated bubble detachment observed by Koza et al. [15]. Moreover, it was
476 theoretically and numerically shown that this lift force and the buoyancy
477 force scale both with the bubble dimension to the third power. Thus the
478 ratio of these forces and the conclusions remain the same even for very small
479 hydrogen bubbles as present in real systems. On the other hand, experimen-
480 tal investigations of the flow generated by an array of magnets, representing
481 a group of bubbles, show the generation of a significant global shear flow
482 which may force an earlier bubble detachment and might therefore offer an
483 explanation for the observations by Koza et al. [15].

484 6. Acknowledgements

485 The financial support from DFG through the Emmy-Noether Research
486 group program under grant No. CI 185/3 is gratefully acknowledged by JM,
487 DB and CC. The authors would also like to thank K. Eckert, M. Uhlemann,
488 G. Mutschke and J. Koza for fruitful discussions. TW appreciates productive
489 discussions with V. Galindo concerning OpenFOAM.

- 490 [1] R. A. Huggins, *Energy Storage: Fundamentals, Materials and Applica-*
491 *tions*, Springer, 2016.
- 492 [2] A. Ursua, L. M. Gandia, P. Sanchis, Hydrogen production from water
493 electrolysis: current status and future trends, *Proc. IEEE* 100 (2012)
494 410–426. doi:10.1109/JPROC.2011.2156750.
- 495 [3] D. Pletcher, X. Li, Prospects for alkaline zero gap water electrolyzers
496 for hydrogen production, *International Journal of Hydrogen Energy* 36
497 (2011) 15089 – 15104. doi:10.1016/j.ijhydene.2011.08.080.

- 498 [4] K. Zeng, D. Zhang, Recent progress in alkaline water electrolysis for
499 hydrogen production and applications, *Prog. Energy Combust. Sci* 36
500 (2010) 307–326. doi:10.1016/j.pecs.2009.11.002.
- 501 [5] F. Hine, M. Yasuda, R. Nakamura, T. Noda, Hydrodynamic studies of
502 bubble effects on the iR-drops in a vertical rectangular cell, *Journal of*
503 *the Electrochemical Society* 122 (1975) 1185–1190.
- 504 [6] B. E. Bongenaar-Schlenter, L. J. J. Janssen, S. J. D. van Stralen,
505 E. Barendrecht, The effect of the gas void distribution on the ohmic
506 resistance during water electrolytes, *Journal of Applied Electrochem-*
507 *istry* 15 (1985) 537–548.
- 508 [7] J. Dukovic, C. W. Tobias, The Influence of Attached Bubbles on Po-
509 tential Drop and Current Distribution at Gas-Evolving Electrodes, *J.*
510 *Electrochem. Soc.* 134 (1987) 331–343. doi:10.1149/1.2100456.
- 511 [8] H. Vogt, R. Balzer, The bubble coverage of gas-evolving electrodes in
512 stagnant electrolytes, *Electrochim. Acta* 50 (10) (2005) 2073 – 2079.
513 doi:10.1016/j.electacta.2004.09.025.
- 514 [9] F. Hine, K. Murakami, Bubble effects on the solution iR drop in a
515 vertical electrolyzer under free and forced convection, *J. Electrochem.*
516 *Soc.* 127 (2) (1980) 292–297.
- 517 [10] C. Sillen, The effect of gas bubble evolution on the energy efficiency in
518 water electrolysis, Ph.D. thesis, TU Eindhoven (1983).
- 519 [11] B. J. Balzer, H. Vogt, Effect of electrolyte flow on the bubble coverage
520 of vertical gas-evolving electrodes, *J. Electrochem. Soc.* 150 (2003) E11–
521 E16. doi:10.1149/1.1524185.
- 522 [12] D. Zhang, K. Zeng, Evaluating the behavior of electrolytic gas bubbles
523 and their effect on the cell voltage in alkaline water electrolysis, *Ind.*
524 *Eng. Chem. Res.* 51 (2012) 13825–13832. doi:10.1021/ie301029e.
- 525 [13] H. Matsushima, T. Iida, Y. Fukunaka, Observation of bubble layer
526 formed on hydrogen and oxygen gas-evolving electrode in a magnetic
527 field, *Journal of Solid State Electrochemistry* 16 (2012) 617–623.
- 528 [14] H. Matsushima, T. Iida, Y. Fukunaka, Gas bubble evolution on transpar-
529 ent electrode during water electrolysis in a magnetic field, *Electrochim-*
530 *ica Acta* 100 (2013) 261–264.

- 531 [15] J. A. Koza, S. Mühlenhoff, P. Żabiński, P. Nikrityuk, K. Eckert, M. Uh-
532 lemann, A. Gebert, T. Weier, L. Schultz, S. Odenbach, Hydrogen evolu-
533 tion under the influence of a magnetic field, *Electrochimica Acta* 56
534 (2011) 2665–2675.
- 535 [16] T. Iida, H. Matsushima, Y. Fukunaka, Water electrolysis under a mag-
536 netic field, *Journal of the Electrochemical Society* 154 (2007) E112–
537 E115.
- 538 [17] Z. Diao, P. A. Dunne, G. Zangari, J. M. D. Coey, Electrochemical noise
539 analysis of the effects of a magnetic field on cathodic hydrogen evolution,
540 *Electrochemistry Communications* 11 (2009) 740–743.
- 541 [18] M. F. Kaya, N. Demir, M. S. Albawabiji, M. Tas, Investigation of alka-
542 line water electrolysis performance for different cost effective electrodes
543 under magnetic field, *International Journal of Hydrogen Energy* (2017)
544 –doi:10.1016/j.ijhydene.2017.02.039.
- 545 [19] J. A. Koza, M. Uhlemann, A. Gebert, L. Schultz, Desorption of hydrogen
546 from the electrode surface under influence of an external magnetic field,
547 *Electrochemistry Communications* 10 (2008) 1330 – 1333.
- 548 [20] J. A. Koza, S. Mühlenhoff, M. Uhlemann, K. Eckert, A. Gebert,
549 L. Schultz, Desorption of hydrogen from an electrode surface under in-
550 fluence of an external magnetic field - In-situ microscopic observations,
551 *Electrochemistry Communications* 11 (2009) 425 – 429.
- 552 [21] D. Baczyzmalski, T. Weier, C. J. Kähler, C. Cierpka, Near-wall measure-
553 ments of the bubble- and lorentz-force-driven convection at gas-evolving
554 electrodes, *Experiments in Fluids* 56 (2015) 162.
- 555 [22] T. Weier, S. Landgraf, The two-phase flow at gas-evolving electrodes:
556 Bubble-driven and lorentz-force-driven convection, *The European Phys-
557 ical Journal Special Topics* 220 (2013) 313–322.
- 558 [23] J. Klausner, R. Mei, D. Bernhard, L. Zeng, Vapor bubble departure in
559 forced convection boiling, *International J. Heat Mass Transfer* 36 (1993)
560 651–662.
- 561 [24] G. Duhar, C. Colin, Dynamics of bubble growth and detachment in a
562 viscous shear flow, *Physics of Fluids* 18 (2006) 077101.
- 563 [25] H. Liu, L. Pan, H. Huang, Q. Qin, P. Li, J. Wen, Hydrogen bubble
564 growth at micro-electrode under magnetic field, *Journal of Electroana-
565 lytical Chemistry* 754 (2015) 22 – 29.

- 566 [26] D. Baczymalski, F. Karnbach, X. Yang, G. Mutschke, M. Uhlemann,
567 K. Eckert, C. Cierpka, On the electrolyte convection around a hydrogen
568 bubble evolving at a microelectrode under the influence of a magnetic
569 field, *Journal of The Electrochemical Society*.
- 570 [27] L. Luo, H. S. White, Electrogeneration of single nanobubbles at sub-
571 50-nm-radius platinum nanodisk electrodes, *Langmuir* 29 (35) (2013)
572 11169–11175.
- 573 [28] X. Yang, F. Karnbach, M. Uhlemann, S. Odenbach, K. Eckert, Dynamics
574 of single hydrogen bubbles at a platinum microelectrode, *Langmuir* 31
575 (2015) 8184–8193.
- 576 [29] D. Fernández, P. Maurer, M. Martine, J. M. D. Coey, M. E. Möbius,
577 Bubble formation at a gas-evolving microelectrode, *Langmuir* 30 (2014)
578 13065–13074.
- 579 [30] D. Fernández, M. Martine, A. Meagher, M. E. Möbius, J. M. D. Coey,
580 Stabilizing effect of a magnetic field on a gas bubble produced at a
581 microelectrode, *Electrochem. Comm.* 18 (2012) 28–32.
- 582 [31] H. Liu, L. Pan, J. Wen, Numerical simulation of hydrogen bubble growth
583 at an electrode surface, *The Canadian Journal of Chemical Engineering*
584 94 (2016) 192–199.
- 585 [32] J. D. Jackson, *Klassische Elektrodynamik*, DeGruyter, 2006.
- 586 [33] H. Knoepfel, *Magnetic fields*, Wiley, 2000.
- 587 [34] C. Cierpka, R. Segura, R. Hain, C. J. Kähler, A simple single camera
588 3C3D velocity measurement technique without errors due to depth of
589 correlation and spatial averaging for microfluidics, *Measurement, Sci-
590 ence & Technology* 21 (2010) 045401.
- 591 [35] C. Cierpka, M. Rossi, R. Segura, C. J. Kähler, On the calibration of
592 astigmatism particle tracking velocimetry for microflows, *Measurement,
593 Science & Technology* 22 (2011) 015401.
- 594 [36] C. Cierpka, B. Lütke, C. J. Kähler, Higher order multi-frame Particle
595 Tracking Velocimetry, *Experiments in Fluids* 54 (2013) 1533.
- 596 [37] H. G. Weller, G. Tabor, H. Jasak, C. Fureby, A tensorial approach to
597 computational continuum mechanics using object-oriented techniques,
598 *Comput. Phys.* 12 (6) (1998) 620–631.

- 599 [38] U. Bödewadt, Die Drehströmung über festem Grunde, Zeitschrift für
600 Angewandte Mathematik und Mechanik 20 (1940) 241–253.
- 601 [39] I. E. Irodov, Basic laws of electromagnetism, Mir, 1986.